Original Article

Design and optimization of Miura-Origami-inspired structure for high-performance self-charging hybrid nanogenerator

Satana Pongampai [a, f], Phakkhananan Pakawanit [b], Thitirat Charoonsuk [c], Sugato Hajra [e], Hoe Joon Kim [e], Naratip Vittayakorn [a, d, *]

[a] Advanced Materials Research Unit, School of Science, King Mongkut's Institute of Technology Ladkrabang, Bangkok 10520, Thailand
[b] Synchrotron Light Research Institute (Public Organization), 111 University Avenue, Muang District, Nakhon Ratchasima 30000, Thailand
[c] Department of Materials Science, Faculty of Science, Srinakharinwirot University, Sukhumvit 23, Watthana, Bangkok 10110, Thailand
[d] Department of Chemistry, School of Science, King Mongkut's Institute of Technology Ladkrabang, Bangkok 10520, Thailand
[e] Department of Robotics and Mechatronics Engineering, Daegu Gyeongbuk Institute of Science and Technology (DGIST), Daegu, 42988 South Korea
[f] Department of Physics, Faculty of Science, King Mongkut's University of Technology Thonburi, 126 Pracha Uthit Rd., Bang Mod, Thung Khru, Bangkok 10140, Thailand

ARTICLE INFO

ABSTRACT

A hybrid piezoelectric-triboelectric-electromagnetic nanogenerator (HPTENG-EMG) has been designed meticulously by focusing on material selection, structural design, and performance evaluation. The module can operate using three parts; piezoelectric, triboelectric and an electromagnetic mechanism. The hybrid concept of triboelectric and piezoelectric is achieved by fabricating triboelectric-piezoelectric composite materials working through the TENG mechanism. In the material design part, the composite film between bacterial cellulose (BC) and BaTiO$_3$ nanoparticles (BT-NPs) fabricates and optimizes its properties with a suitable number of BT-NPs. The unique Miura-Origami (MO) hexagonal multilayer shape is applied within the structural design to increase the contact surface area, which enhances the electrical output signal. The third part of the hybrid system incorporates an electromagnetic generator (EMG) by designing a structure of compact and lightweight cylindrical tubes with magnetic levitation structures. The hexagonal multilayer shape of MO composite TENG (MO-CTENG) generates an open-circuit output voltage (V_{OC}) of ~414 V and short-circuit output current (I_{SC}) of ~48.3 μA with maximum output power (P) of about ~6.94 mW. The highest I_{SC} value of ~38 mA can be promoted in the optimized EMG, which is higher than the MO-CTENG by ~786 times. The practical application of this technology is demonstrated by human shaking motion for battery charging in the wireless Global Positioning System (GPS). The maximum direct current output voltage (V_{DC}) saturation of 30 V can be achieved within 19 s. This work provides a potential methodology for increasing electrical output performance by capturing more mechanical energy through the conjunction of three phenomena into a single device, which exhibits a promising way of addressing an energy crisis.

1. Introduction

The advent of intelligent networks and the merging of IoT with AI are rapidly advancing [1], bringing forth new technologies such as mobile terminals, wearable electronics, and smart sensors. However, these new generation devices face a challenge in terms of

their power supply. Traditional lithium-ion batteries, with their frequent charging and replacement needs, are not suitable for providing a reliable and sustainable power source. To overcome this limitation, sustainable energy technologies have been developed to harvest energy from various sources, including ocean waves [2], wind [3], geothermal devices [4], solar power [5,6], vibrations [7], and human activity [8]. Among the various energy harvesting technologies, mechanical energy harvesting (MEH) has emerged as one of the most promising technologies for powering small electronic devices and sensors. MEH systems convert mechanical energy from vibrations, motion, and rotation into electricity using

nanogenerators [9]. There are three main types of nanogenerators: piezoelectric nanogenerators (PENG) [10,11], electromagnetic nanogenerators (EMG) [12,13], and triboelectric nanogenerators (TENG) [14]. Each of these nanogenerators has its own set of benefits. PENG mainly uses piezoelectric materials to transform mechanical stress or strain into electrical energy [15] offering stable and high electrical output with excellent resistance to humidity [10]. EMG uses electromagnetic induction [16], exhibiting high output performance at high frequencies [17,18]. TENG, on the other hand, utilizes triboelectrification and electrostatic induction [9], and it stands out due to its low cost, lightweight construction, flexible design, and ability to achieve high efficiency at low frequencies.

Despite their individual advantages, each energy harvesting technology still has limitations that need to be addressed. For instance, PENG generates low output current due to the high impedance of the piezoelectric materials, and the efficiency of PENG is limited by the properties of the materials used. TENG functions as a low current source with high parallel internal impedance, and its practical applications are affected by varying charge density on the triboelectric layer and environmental factors such as abrasion, humidity, and temperature. EMG behaves as a low-voltage generator with low internal impedance, but it exhibits low open-circuit output voltages [19]. To overcome these limitations and maximize energy harvesting efficiency, sensitivity, and durability, a hybrid strategy between TENG and PENG, as well as TENG and EMG, has been proposed [20–22]. By taking advantage of each other's strengths, the development of hybrid piezoelectric-triboelectric-electromagnetic nanogenerators (HPTENG-EMG) offers a promising solution beyond the performance of individual mechanisms for enhancing the nanogenerator performance in practical self-powered sensors and energy harvesters.

In this study, our objective is to investigate the HPTENG-EMG hybridized technology through material selection, structural design, and performance evaluation, with a particular focus on developing an efficient fabrication process suitable for mass production. To achieve the hybrid concept of TENG and PENG, we employ polymer-composite triboelectric-piezoelectric materials operating through the TENG mechanism. Specifically, we fabricate eco-friendly bacterial cellulose (BC) and commercial BaTiO₃ nanoparticles (BT-NPs) or BC/BT-NPs composites. For the structural design, we utilize the innovative Miura-origami-inspired TENG [23]. By folding the BC/BT-NPs composite film into the Miura-origami structure (MO-CTENG), we can create stacked hexagonal multilayer TENGs, transforming a 2D sheet substrate into a complex 3D structural TENG. This hexagonal multilayer shape MO-CTENG significantly amplifies the contact triboelectrification effect and the capacitance variation of electrostatic induction by increasing the contact surface area. In the hybridization process, we incorporate the MO-CTENG into an EMG module, resulting in the MO-CTENG-EMG hybrid system. The EMG module consists of four hollow cylindrical tubes with wrapped copper wire, carefully designed to ensure compactness, lightweight construction, and replaceability. Through meticulous design and optimization of each component, the MO-CTENG-EMG is well-assembled to be operated simply by shaking using a hand. The performance of the hybrid system is evaluated by its ability to charge batteries in wireless Global Positioning System (GPS) applications. This work represents an innovative approach toward effective mechanical energy harvesting and presents an excellent prospect for the fabrication of intelligent self-powered wireless GPS systems. By addressing the limitations of individual energy harvesting technologies and combining their strengths, the HPTENG-EMG hybridized technology holds great potential for advancing the field of energy harvesting and enabling the development of sustainable and self-powered electronic devices.

2. Experimental

2.1. Preparation of bacterial cellulose (BC) composite film

Commercial coconut jelly was used as raw material for synthesizing the BC composite film. First, the boiling process in deionized (DI) water was used to separate sugar syrup at 80 °C for 12 h, with the DI water changed every 1 h to prevent a saturated solution. After 12 h, the boiled water was validated with a benedict solution to ensure that residual syrup was eliminated. Second, the BC was blended and centrifuged to separate the BC fibers from water, and then the separated BC fibers were stirred with ethanol. Barium Titanate Nanoparticles (BT-NPs) were dispersed in BC solution by varying the number of BT-NPs fillers by 1, 5, 10, 20, 30, 40 and 50 wt% to form the suspension. Finally, the BC composite films were obtained by evaporating the solvent at 55 °C for 24 h. The BC-based films were obtained with a thickness of ~120 μm. The composite film was poled at 40 kV/cm for 30 min before being assembled into the device.

2.2. Fabrication of the hexagonal multilayer-shaped MO-CTENG

Transferring the hexagonal multilayer-shaped MO-CTENG for device fabrication was inspired by the folding process of the ancient art of MO. Fig. 1(a) exhibits the parallelogram of woodfree paper (270 mm thickness) with a dimension of 25 × 11.5 cm². The cutting line (yellow-dashed) shows the boundary of the active area that forms the tessellation of the surface. Gray highlight and diagonal black dashes on the left and right sides demonstrate the active area of tribomaterial pairs and the wasted area, respectively. Fig. 1(b) shows detail of the folding process and assembly of the MO-CTENG unit. The blue and red dashed lines denote valley and mountain folds, respectively. The valley and mountain creases were folded alternately from one side to the next to form a zigzag path through the horizontal axis (y-axis). The dimension in each cell of the MO-CTENG unit (in the purple dashed square line) is defined by the height, width and vertex angle (θ) of 10 cm, 5 cm and 55°, respectively. Hence, planar of the MO-CTENG from woodfree paper can be compressed into a 3D multilayer shape by pressing on two opposite sides, and similarly uncompressing by stretching on two opposite ends. In order to increase the contact surface area significantly, two units of the MO-CTENG were assembled by alignment of mirror-image sticking with adjacent facets, according to the inset of Fig. 1(b). Then, an acrylic substrate was stuck to hold them like a hexagonal multilayer shape, and another side was stuck by commercial polyimide tape film (Kapton; KT) to hold a rigid structure. Each MO-CTENG unit consists of two planar sides (inside and outside) with a couple of 18 tribomaterial pairs on each one. The inside and outside areas equate to 135 and 253.8 cm², respectively. Therefore, the entire contact surface area of the hexagonal multilayer-shaped MO-CTENG is equal to ~778 cm². Fig. 1(c) shows the dimensions of tribomaterial materials and assembled layers with patterned copper (Cu) wire. The Cu wire was used to bond with the conductive electrode layer, which was fabricated from commercial aluminum (Al) tape of 90 μm thickness. The red and blue Cu wires denote the polytetrafluoroethylene (PTFE) and BC/BT-NPs sides, respectively. Afterward, the tribomaterial pairs (PTFE and BC/BT-NPs) were cut to the same dimensions as the Al conductive electrode and then stuck face-to-face. On the contrary, the inside planar of the MO-CTENG was fabricated similarly to the outside one. Finally, the Cu wire of the BC/BT-NPs and PTFE sides from two MO-CTENG units were connected in parallel mode.
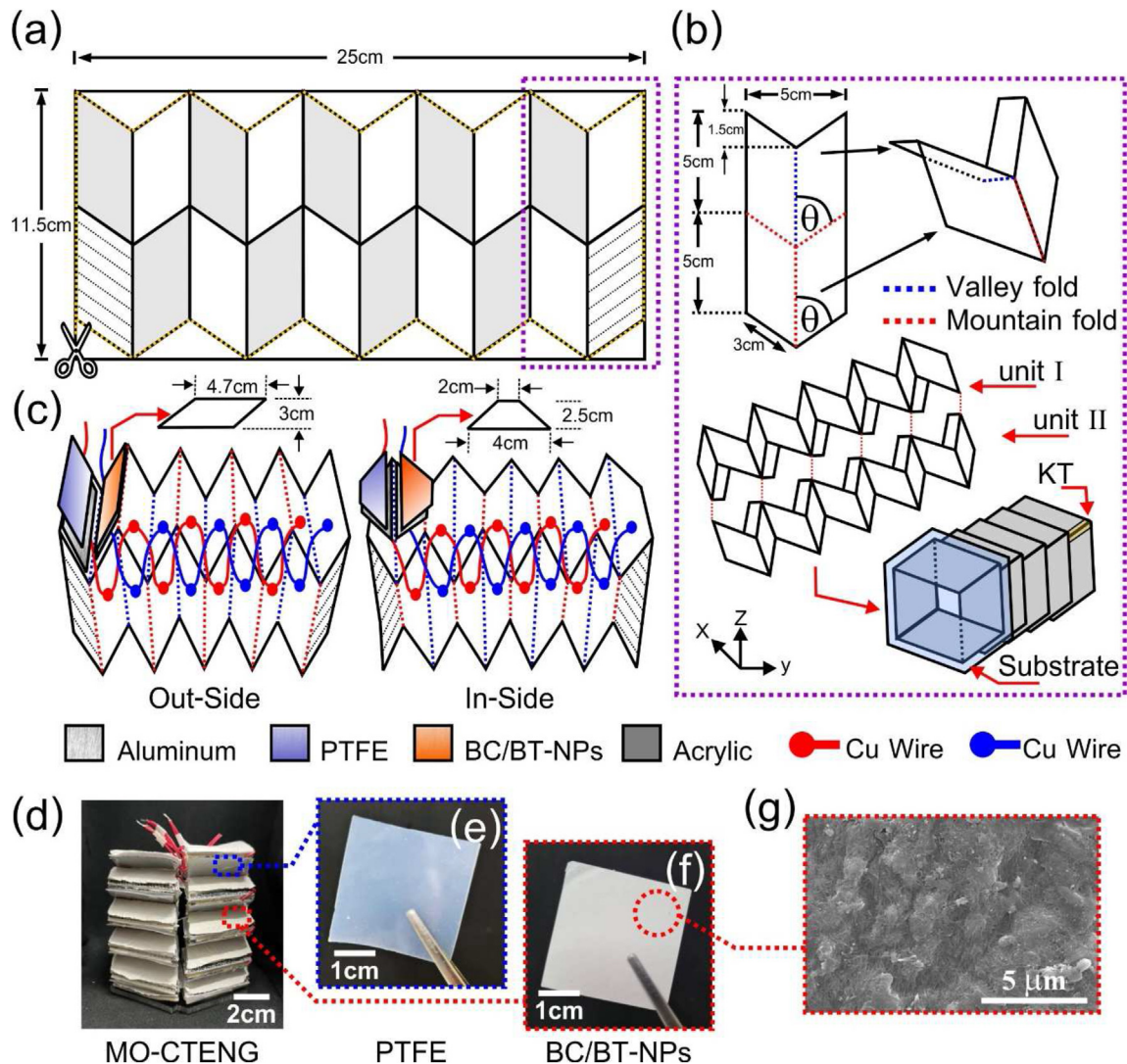
Fig. 1. Fabrication process of the MO-CTENG; crease pattern of the MO-CTENG with parallelogram frame of woodfree paper (a), folding process and assembly of two MO-CTENG units (b), dimension of tribomaterial pairs and assembled layers with patterned Cu wire (c), photograph of the assembled hexagonal multilayer shape MO-CTENG (d), PTFE film (e), BC/BT-NPs film (f), and morphology of the BC/BT-NPs composite film by SEM characteristic (g).

Fig. 1(d) shows the fabricated prototype of the hexagonal multilayer-shaped MO-CTENG. Fig. 1(e) and (f) exhibit the real photograph of the PTFE and BC/BT-NPs film, respectively, from a digital camera. Fig. 1(g) shows morphology of the BC/BT-NPs composite film by scanning electron microscope (SEM) characterization.

2.3. Fabrication of the EMG

Fig. 2(a) shows the structural design with a dimension of EMG fabrication. The EMG structure was made from polyvinyl alcohol (PVA) filament by 3D print technology. Dimension of the bottom substrate is 5×5 cm^2, with a 1.5 cm thickness. Each corner of the bottom substrate was constructed with a hollow cylindrical tube (7 cm in length) that had an outer and inner radius of 1.6 and 1.2 cm, respectively. In order to wrap and align the Cu wire onto the hollow cylindrical tube easily, a groove of 2.5 cm in length and 0.15 cm depth was made, as shown on the side-view in Fig. 2(a). Then, the Cu wire, with a radius of 0.146 mm, was turned (clockwise direction) about 60 Ω or 1000 turns in each hollow cylindrical tube. Four Neodymium permanent magnets, with a radius of 1 cm and

1.5 cm in length, were used inside the hollow cylindrical tube for inductive current generation by magnetic levitation structure when passing through turned Cu coils. They were set inside the hollow cylindrical tube by alternating magnetic field directions, according to Fig. 2(b). Therefore, the Neodymium permanent magnet could move freely inside the hollow cylindrical tube during external force vibration. Furthermore, the opposite magnetic field direction would help in increasing movement velocity. Fig. 2(c) exhibits the prototype EMG device from a digital camera.

2.4. Electrical output measurement

Supplementary Fig. S1 illustrates the contact-separation mode, wherein the Auto Compressing Machine (ACM) was employed to gather electrical output of the devices. To assess the energy harvesting system, the experiments were conducted at room temperature (RT = 25 ± 2.0 °C). The ACM operation was controlled via a Programmable Logic Control (PLC) integrated with a pneumatic system operating at approximately 6 bar. The mechanical force and frequency were maintained at a constant level of 150 N and 2−3 Hz, respectively. The humidity level inside the testing cabinet was
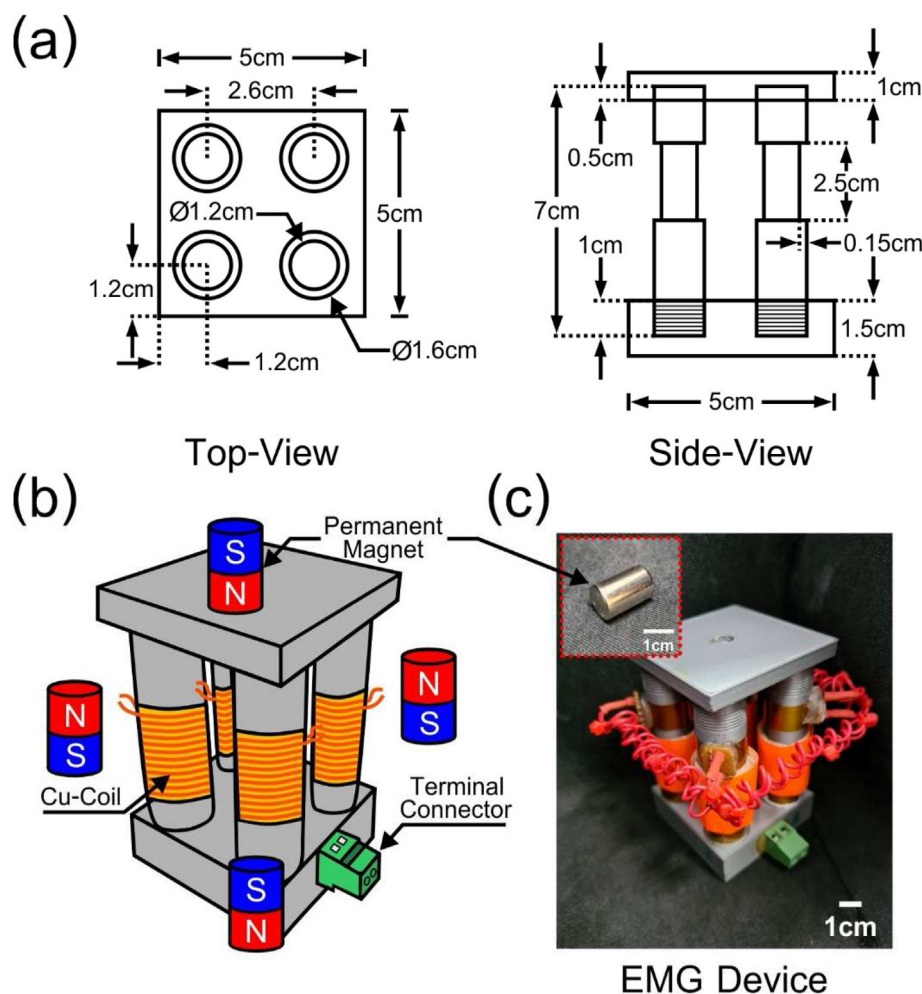
Fig. 2. Fabrication process of the EMG for scavenging mechanical energy; designed dimension of the EMG (a), schematic diagram of the EMG (b), and prototype of the EMG from a digital camera (c).

regulated to below 50 ± 5 %RH. In addition, the mechanical frequency used for studying the electrical output characteristics could be adjusted by initiating triggers from the PLC. The V_{OC} waveform analysis was collected by a digital storage oscilloscope (DSO-X 2012A, Keysight). The I_{SC} was collected via the DSO by transmitting an ultra-low input current amplifier (LMC6001, Texas Instruments) circuit. The circuit diagram is shown in Supplementary Fig. S2. Moreover, the other electrical output waveforms; i.e., stability, direct voltage/current output at various load resistances, maximum output P, and chargeability, were analyzed systematically. Finally, the practical application (self-charged wireless GPS) also validated the electrical output performances in terms of real application.

3. Results and discussion

3.1. Characterization of bacterial cellulose BC/BT-NPs composite film

BT-NPs characteristics were investigated, as shown in Fig. S3 of the supplementary information. The X-ray diffraction (XRD) peaks occurring in Fig. S3 (a) correspond to the single phase of perovskite BaTiO3. All of the peaks match well with the XRD pattern of cubic (*Pm3m*) structure, corresponding to the standard data in JCPDS file number #892475. The lattice parameter ($a = b = c$) and crystalline size were calculated and found to be 4.017 ± 0.012 Å and

60.8 ± 1.6 nm, respectively. The related structural model was created by Visualization for Electronic and Structural Analysis (VESTA) software, as presented in Fig. S3 (b). However, the XRD pattern showed cubic phase stabilization. Analysis with Raman spectroscopy [Fig. S3 (c)], which is more sensitive to lattice distortions and crystallographic defects, confirms stability of the tetragonal (*P4mm*) distortion in the unit cell. The notable feature of longitudinal and transverse optical vibration by [B1, E(TO3 + LO2)] and [E(TO4) + A1(LO2)] modes were observed, thus indicating the characteristic of ferroelectric materials. Also, the existence of characteristic peaks from local displacement of the Ti atom and asymmetric O−Ti−O in TiO6 by A1(TO2), [E(TO4), A1(TO3)] and [E(LO4) + A1(LO3)] modes were identified. Therefore, the Raman result can confirm the asymmetric structure by lattice distortions in BT-NPs, resulting in the ability to create polarization when adding to the BC matrix. The average particle size of BT-NPs in this work was found to be 122 ± 11 nm, as presented by the SEM image in Fig. S3 (d). After making composite, the films were characterized and results are shown in Fig. 3. According to the XRD results [Fig. 3 (a)], the X-ray peak pattern of BC from the coconut jelly, without adding BT-NPs, suggested its crystalline nature. The relative XRD peak positions are in close agreement with the BC produced by Acetobacter xylinum 0416 and *Acetobacter pasteurianus* on Hestrin-Schramm (HS) medium. The invariant peaks indicated by (100), (010) and (110) crystallographic planes are attributed to the
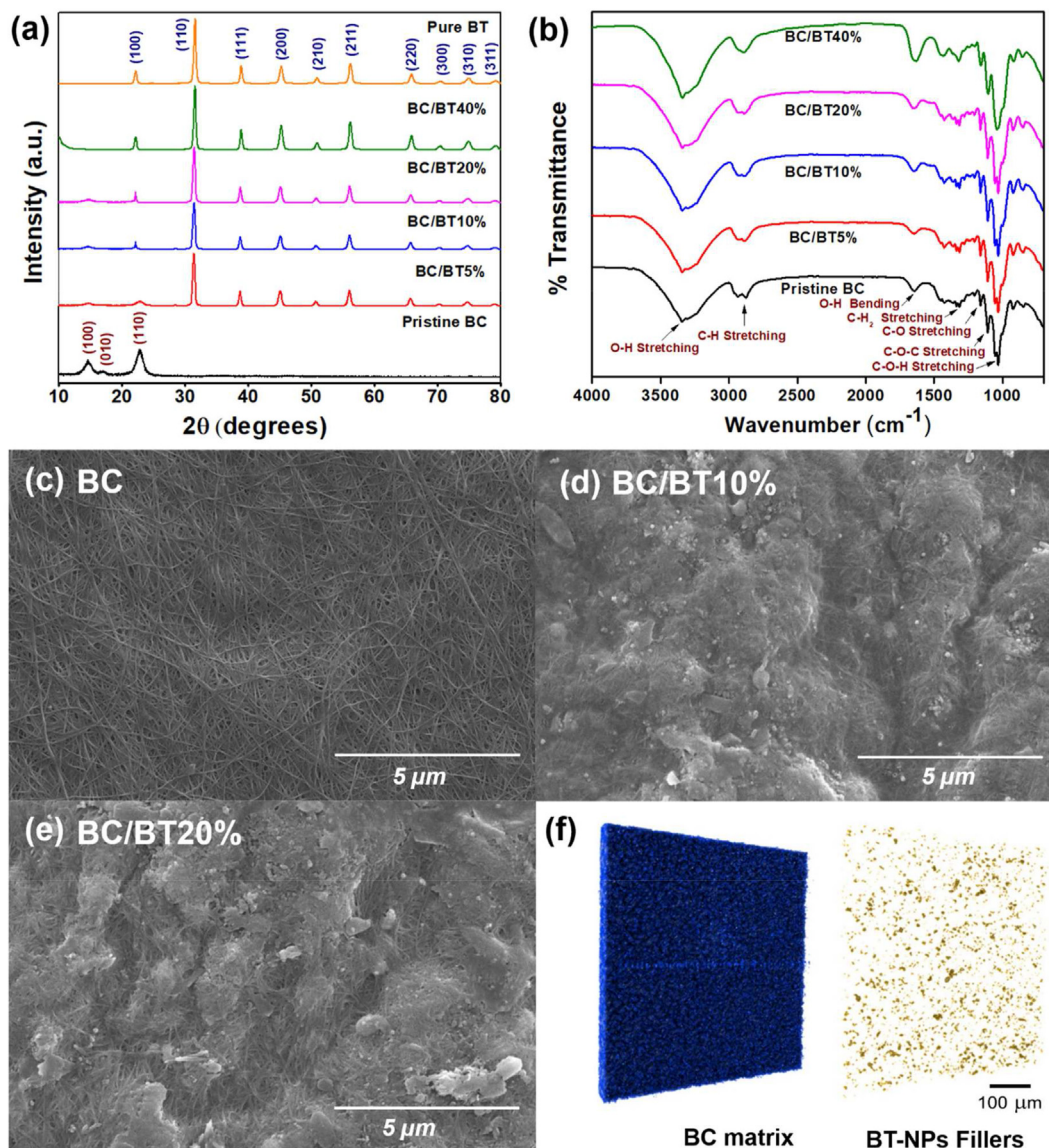
Fig. 3. XRD pattern (a), IR spectra (b), SEM images of BC/BT-NPs composites with various amounts of BT-NPs (c)–(e), and X-ray Tomography Microscopy (XTM) analysis of the BC/BT-NPs 10 wt% composite film (f).

orientation of I_α referring to the triclinic unit cell in the BC chain [24]. After adding BT-NPs at 5–40%, peaks corresponding to the BT-NPs phase are observed clearly, whereas the XRD peak of the BC phase is still apparent. This confirms that compositing between BC and BT-NPs was fabricated successfully. The chemical bonding of BC with the number of BT-NPs was characterized by attenuated total reflection infrared (ATR-IR) spectroscopy, as seen in Fig. 3 (b). All characteristic peaks corresponding to the cellulose structure, including absorption bands of O−H stretching at 3400−3200 cm^{-1} O−H bending at 1650-1600 cm^{-1}, C−H stretching at 2944 cm^{-1} (CH-) and 2878 (CH$_3$-), CH$_2$ stretching at 1410 cm^{-1}, and skeleton of C−O, C−OC and C−O−H vibration ranging between 1110 and 1230 cm^{-1}, can be observed in all conditions [25]. The existence of BT-NPs in the BC matrix cannot be detected by ATR-IR spectroscopy because the metal oxide (M−O) vibrational modes normally occur at a lower wavenumber than 700 cm^{-1}. The SEM images in Fig. 3(c−e) show that the BT-NPs found on the BC matrix were proportional directly to the number of BT-NPs. Not only SEM investigation, but also the X-ray tomography microscope (XTM)

with Synchrotron light radiation, providing a 3D virtualization image, can confirm incorporation of well-distributed BT-NPs inside BC. The 3D image of the BC/BT-NPs 10% composite film is presented representatively in Fig. 3 (f). It can be seen that BT-NPs were not only stuck on the surface, but also incorporated inside the BC matrix with homogeneous dispersion, identified by using different color. The absorption area of BC is indicated in blue, and the BT-NPs dispersive phase in brown. Whereas, when adding more than 10%, the BT-NPs agglomerate, especially on the edge of the composite film, as shown in Supplementary Fig. S4. To confirm this assumption, all of the electrical properties are investigated systematically in the next section.

3.2. Mechanical energy harvesting and working principle

Regarding the working principle of the HPTENG-EMG phenomena, the electrical power generation process displayed in Fig. 4 can be explained from two main parts, namely the TENG/PENG and EMG effects. First is the triboelectrification and electrostatic
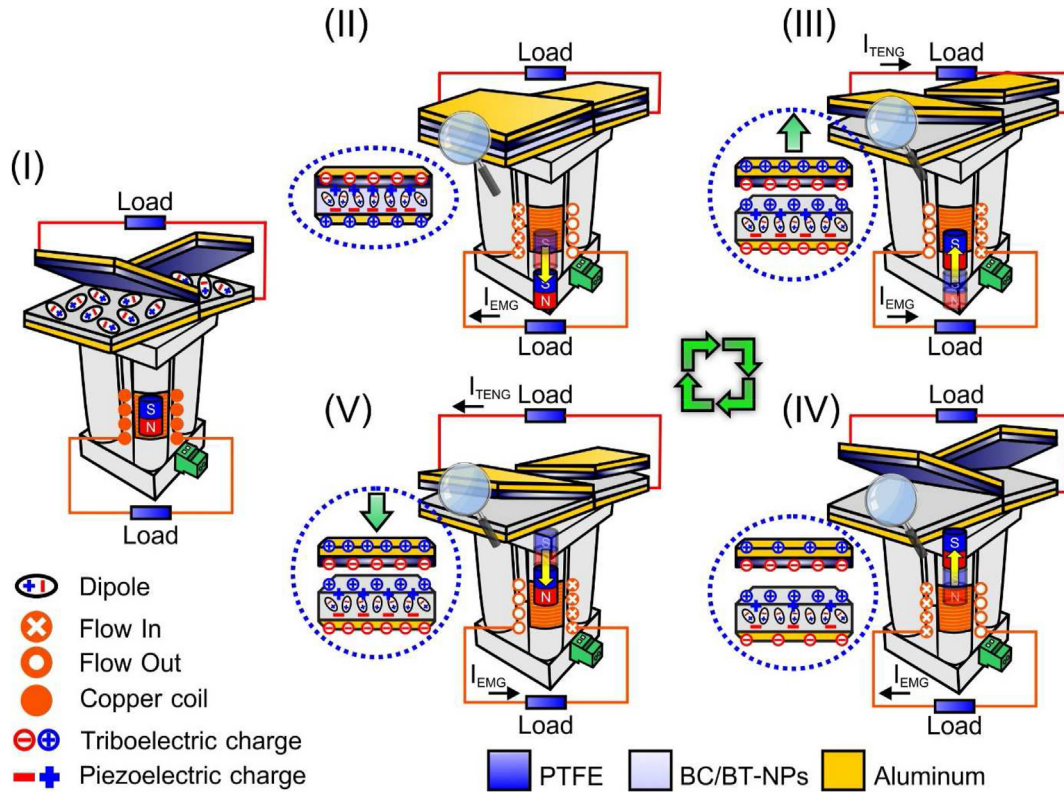
Fig. 4. Working principle of the hybrid piezoelectric-triboelectric-electromagnetic nanogenerator (MO-CTENG-EMG) phenomena.

induction in vertical contact-separation mode in a V-shape structure [26], including the piezoelectric charge induction inside the BC/BT-NPs composite film during the compressing stage. Second is inducing the current flow by Faraday electromagnetic induction from changing magnetic flux (φ) intensity to Cu coil by a magnetic levitation structure or freestanding cylindrical magnet. This coupling behavior can improve the entire electrical output performance of this work. To describe the power generation process easily, the hexagonal multilayer-shaped MO-CTENG served only the first bottom layer. It is assumed that each layer of tribomaterial pairs is contacted simultaneously with an approximated capacitance of an idealistic parallel plate capacitor. Similarly, the EMG served only one unit of the hollow cylindrical tube. The cooperative working mechanism of the TENG/PENG and EMG for electrical signal waveform generation is explained in detail by five stages. At the initial stage (stage I), a permanent magnet is provided in the center of the hollow cylindrical tube, including the tribomaterial pairs (PTFE film and BC/BT-NPs composite film) that do not make contact in each layer. As a result, there is no electrical output transferred to an external load of either effect: TENG/PENG and EMG, due to an equilibrium of the potential between tribomaterial pairs, and there is no piezoelectric charge generation because of no deformation of the BC/BT-NPs composite film. Similarly, there is no inductive current flow in the Cu coil, due to no magnetic flux variation. By applying an external vibration (stage II), the tribomaterial pairs make complete contact with the permanent magnet and move downward at the bottom of the Cu coils. As a result, the surface charges are generated by the electrification phenomenon from an electronegativity difference and joining the piezoelectric charges. At the same time, magnetic flux variation occurs through the Cu coil, resulting in inductive current (I_{EMG}) flow through the external load by Lenz's law. When applying an external force in the opposite direction, as shown in stage III, the tribomaterial pairs in

each layer are separated, resulting in an internal potential generation in the electrode pairs, due to the electrostatic induction phenomenon. The tribo/piezo charges flow through an external load until the electrical potential balances (equilibrium state) and the cycle is completed in stage IV. Meanwhile, the permanent magnet goes backwards (passing into the Cu coil). As a result, the I_{EMG} is generated in the opposite direction and flows through the external load. As in the cooperative working mechanism in stage IV, when the permanent magnet moves upward, I_{EMG} is induced in the opposite direction. Finally, when applying an external force again, the induced charge (the tribo/piezo charges are recovered) and I_{EMG} flow back to the external load with opposite charges (stage V). During continuous external force vibration, electrical output is obtained, and it flows to an external load as alternating current (AC).

3.2.1. Output performance of the hexagonal multilayer-shaped MO-CTENG

In order to study the influence of electrical output performance on various amounts of BT-NPs filler inside BC film, crucial parameters were controlled carefully for all experiments. Fig. 5(a) shows the ACM and device structure with a dimension of the BC/BT-NPs composite film to validate electrical output performance. The ACM conditions were controlled similarly to the electrical output measurement section. The device structure was fabricated from an acrylic sheet with freestanding movement in vertical direction. The bottom acrylic sheet was fixed by four nuts and long-screws, before applying four metal springs to the inner long-screw for rebounding the top acrylic sheet during separation motion. All tribomaterial pairs were prepared at the dimension of 3×3 cm^2, similar to the conductive Al electrodes. Finally, the Cu wire was inserted under the conductive Al electrode for an electrical output signal measurement. Fig. 5(b) and (c) exhibit the correlation of V_{OC} and I_{SC} on
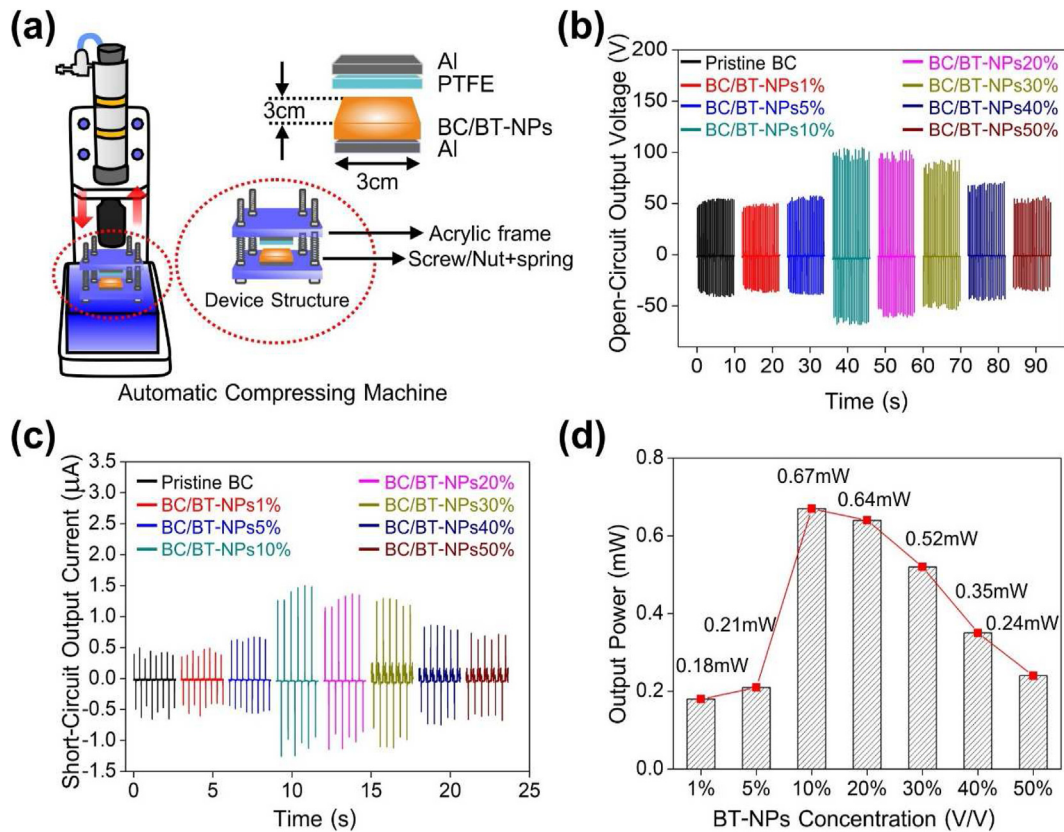
Fig. 5. ACM and device structure diagram with dimension of the BC/BT-NPs composite film (a), open-circuit output voltage (b), short-circuit output current (c), and maximum output power (d) of various amounts of BT-NPs fillers inside BC composite film.

various numbers of BT-NPs fillers inside the BC film (1, 5, 10, 20, 30, 40, and 50 wt %). The V_{OC} and I_{SC} were increased with an increasing number of BT-NPs fillers, due to enhancing relative permittivity. Until the concentration of BT-NPs reaches 10%, significant improvements in V_{OC} and I_{SC} are observed, with values of 104 V and 1.5 μA, respectively. These values represent a two-fold and three-fold increase compared to the pristine BC film. However, as the weight percentage of BT-NPs filler exceeds 10 wt%, both V_{OC} and I_{SC} gradually decline. This decrease can be attributed to the poor distribution and agglomeration of BT-NPs within the BC matrix, as confirmed by XTM analysis in the previous section. To gain a deeper understanding of this phenomenon, it is important to consider the percolation threshold, which determines the optimal balance between the matrix and filler in the composite. In this case, the percolation threshold is identified as 10%. Above this threshold, the improper distribution and agglomeration of BT-NPs disrupt the uniform dipole orientation, resulting in weakened inductive charges and diminished electrical output signals. This explanation is also elaborated upon in the author's previous work [27–29]. Another factor contributing to the percolation effect is the limitation imposed by air breakdown phenomena, which affects dielectric charge generation. During the TENG mechanism, positive charges are generated on the BC friction surface, and subsequently, negative charges are induced on the electrode. These charges accumulate at that point temporarily, creating a small electric field. The incorporation of BT-NPs can be likened to the presence of microcapacitors within the BC friction layer, allowing for increased electron trapping and enhanced charge density. Reaching the air breakdown limitation yields the highest dielectric constant, resulting in the highest electrical output. However, surpassing the air breakdown limitation by adding an excessive number of BT-NPs

leads to the loss and recombination of electric charges, thereby reducing the electrical signal. This percolation effect, which related to both dielectric and air breakdown phenomena, also is discussed elsewhere [27,30,31]. In Fig. 5(d), the trend of maximum output power is presented for different concentrations of BT-NPs filler within the BC film. The electrical output performance follows a similar pattern to V_{OC} and I_{SC}, indicating that the BC/BT-NPs composite film with 10 wt.% exhibited outstanding electrical output characteristics. Hence, it can be concluded that the BC/BT-NPs composite film at 10 wt.% represents the optimal condition.

In general, the basic TENG structure for contact-separation mode could be divided into two categories: dielectric-to-dielectric and conductor-to-dielectric types. The built type for this work is dielectric-to-dielectric type, and the crucial equation based on theory for explaining the real-time power generation is the relationship of three parameters: the voltage (V) between two conductive electrodes, the amount of transferred charge (Q), and the separation distance (x) between the two tribomaterial pairs. It could be named the V-Q-x relationship [32]. The structure of this work could be simplified, as the three capacitors were connected in series mode. Based on Gauss theorem [33], the electric field strength (E) at each region of the capacitor node is obtained from $E_{PTFE} + E_{air} + E_{BC/BT-NPs}$. Therefore, the V-Q-x relationship is unified, as in the following equation.

$$V = -\frac{Q}{S\varepsilon_0}\left(\frac{d_{PTFE}}{\varepsilon_{PTFE}} + \frac{d_{BC/BT-NPs}}{\varepsilon_{BC/BT-NPs}} + x(t)\right) + \frac{\sigma x(t)}{\varepsilon_0} \qquad (1)$$

where S and σ are the contact surface area of the conductive electrode and opposite static charges (tribo-charges) density,

respectively. Q is an induced charge, and ε_0, ε_{PTFE}, and $\varepsilon_{BC/BT-NPs}$ are permittivity of vacuum, relative permittivity of the PTFE, and BC/BT-NPs composite film, respectively, and d_{PTFE} and $d_{BC/BT-NPs}$ are the PTFE and BC/BT-NPs composite film thickness, respectively. Finally, the intrinsic output characteristics: V_{OC}, I_{SC}, and capacitance (C) can be obtained as follows [34]:

$$V_{OC} = \frac{\sigma x(t)}{\varepsilon_0} \tag{2}$$

$$I_{SC} = \frac{S\sigma d_0 v(t)}{(d_0 + x(t))^2} \tag{3}$$

$$C = \frac{S\varepsilon_0}{d_0 + x(t)} \tag{4}$$

where x(t) is the relative distance between two tribomaterial pairs, v(t) is the relative velocity of tribomaterial pairs, and d_0 is defined as the effective thickness constant given by $\frac{d_{PTFE}}{\varepsilon_{PTFE}} + \frac{d_{BC/BT-NPs}}{\varepsilon_{BC/BT-NPs}}$. Based on the equation of theoretical study, tribo-charges density (σ) and relative permittivity (ε_r) of tribomaterial pairs were revealed dominantly as significant parameters for improving the electrical output performance of the TENG [35]. The dielectric property versus frequency dependence (1−1 MHz) was measured by LCR meter at RT which is shown in Supplementary Fig. S5. It can be observed that pristine BC demonstrates the lowest relative permittivity. When adding BT-NPs fillers inside the BC matrix, the relative permittivity increases significantly, and the optimum condition for BC/BT-NPs 10 wt.% exhibits the highest value.

Moreover, another significant factor is the contact surface area, which corresponds with equations (3) and (4). It is directed proportionally to the I_{SC} and C for increasing electrical output performance. The entire contact surface area of one MO-CTENG unit exhibits 388.8 cm^2, which is divided into two planar sides: the inside of 135 cm^2, and outside of 253.8 cm^2. Finally, the hexagonal multilayer-shaped MO-CTENG is equal to ~778 cm^2. Hence, the implementation of hexagonal multilayer-shaped MO-CTENG demonstrates a significant enhancement in electrical output performance, primarily attributed to the increased contact surface area. As depicted in Fig. 6(a) and (b), the electrical output characteristics (V_{OC} and I_{SC}) of each unit, both inside and outside the MO-CTENG, are presented. The contact surface area within each unit yields V_{OC} values of 84 V (inside) and 104 V (outside), together with 114 V (inside) and 122 V (outside). Similarly, the contact area within each unit delivers I_{SC} values of 11.6 μA (inside) and 13.5 μA (outside), as well as 14.1 μA (inside) and 14.8 μA (outside). After connecting the output terminal wire of the two MO-CTENG units in parallel connection (hexagonal multilayer shape MO-CTENG), according to Fig. 6(c), the V_{OC} and I_{SC} were exhibited dominantly at ~ 414 V and ~48.3 μA, respectively, which improved the V_{OC} and I_{SC} by 3.5 and 3.3 times, respectively, when compared to the average value of V_{OC} and I_{SC} from outside the contact surface area of one MO-CTENG. Electrical output characteristic has shown significant improvement in terms of V_{OC}, which has a tendency to charge an external battery sufficiently. However, it might take a long time to charge a small battery because the I_{SC} still displayed poor efficiency, which affects the charging time for a battery capacity of 250 mAh, as in the design of this work. To address this issue, a designed EMG device would be performed to promote the electrical output characteristic, which is mentioned in the next section.

Finally, the instantaneous output power (P), with analysis of different external load resistances is illustrated in Fig. 6(d). The direct current output voltage (V_{DC}) increased when the external load resistance increased. Meanwhile, the direct output current (I_{DC}) decreased, which corresponded to Ohmic law. The maximum output P was calculated from the relationship of IV, and it exhibited the maximum value of ~6.94 mW at 6 MΩ of the external load resistance. Therefore, it could be concluded that the relationship between the contact surface area and electrical output performance was exhibited clearly in terms of enhancing the electrical output characteristic.

3.2.2. Output performance of the EMG

Results of the electrical output characteristic in the hexagonal multilayer-shaped MO-CTENG revealed that the I_{SC} displayed rather poor efficiency, which directly affected charged ability in terms of charging time. Therefore, in order to promote charged ability, the EMG was proposed to address this issue. The electrical output performance of the hollow cylindrical tube was investigated systematically. Regarding Faraday's law, the V_{OC} and I_{SC} can be expressed by inducing electromotive force (EMF) quantification when the magnetic flux intensity (φ) passes through the Cu coil, as follows.

$$V_{OC} = -N\frac{d\varnothing}{dt} \tag{5}$$

$$I_{SC} = \frac{V_{OC}}{R} \tag{6}$$

where $\varnothing$ is the magnetic flux intensity and N is the number of turns in the Cu coils. R is the internal resistance of the Cu coil. Fig. 7(a) exhibits relationship between the maximum output of V_{OC} and number of turns in the Cu coils. It can be found that the maximum output of V_{OC} has a linear relationship to N, which demonstrates 2.65 V at 1200 turns of the Cu coils. However, the structural design of the hollow cylindrical tube, with a groove length of 2.5 cm, and 0.15 cm depth, and Cu coil diameter of 0.146 mm, is appropriate for N of 1000 turns, due to convenient assembly. With N of 1000 turns, the Cu coil could turn in the designed hollow cylindrical tube if assembled properly. Besides structural designs, the entire output power generation of the EMG is sufficient for driving the GPS (GY-NEO-6MV2 model) module, when it is integrated into 4 hollow cylindrical tubes, like a fabrication design (the GY-NEO-6MV2 module requires power consumption for a direct current of ~10 mA). Also, it shows the advantages of a portable device due to minimizing the weight of the Cu coil. Therefore, N of 1000 turns was selected to investigate the electrical output performance further. To demonstrate the influence of electrical output on N in the Cu coils, and variation of the mechanical working frequency, a hollow cylindrical tube was used for this study. Fig. 7(b) shows the relationship between the maximum output of V_{OC} and various mechanical working frequencies. The maximum output of V_{OC} increases with increasing mechanical working frequency, and then immediately decreases after the frequency of 5 Hz. As a result, it might be noted that the maximum output of V_{OC} corresponded to the resonant frequency at ~5 Hz, when the simple harmonic motion was assumed. Fig. 7(c) and (d) demonstrate the V_{OC} and I_{SC} of each hollow cylindrical tube at the mechanical working frequency of 2−3 Hz. The signal waveform of the V_{OC} and I_{SC} exhibited an insignificant change in all hollow cylindrical tubes. The average output of V_{OC} shows 1.93, 1.96, 1.94 and 1.94 V from the hollow cylindrical tube unit 1, 2, 3 and 4, respectively. Also, the average output of I_{SC} shows 9.7, 10.3, 10.1 and 9.9 mA from the hollow cylindrical tube unit 1, 2, 3 and 4, respectively.

Afterward, each hollow cylindrical tube was assembled in a single device on the designed bottom substrate in order to enhance electrical output current by connecting the output terminal wire in
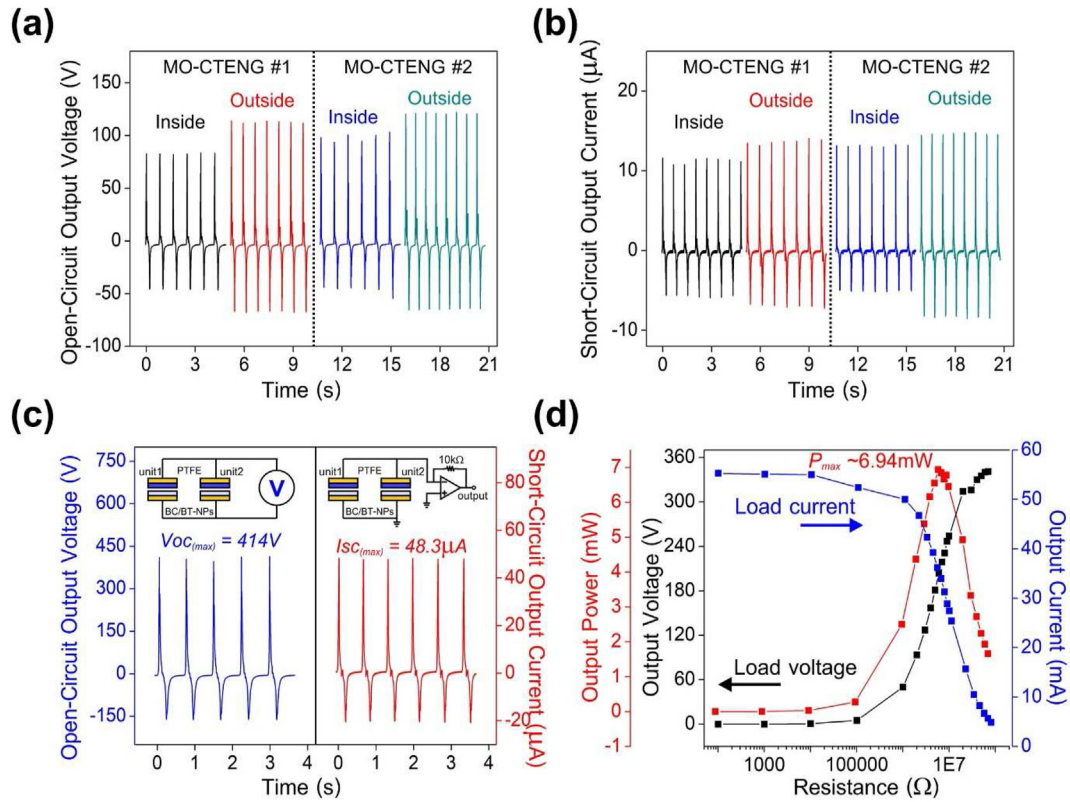
Fig. 6. Open-circuit output voltage (a), short-circuit output current of each MO-CTENG unit (b), open-circuit output voltage and short-circuit output current (c), and the instantaneous output power (d) of the hexagonal multilayer-shaped MO-CTENG.
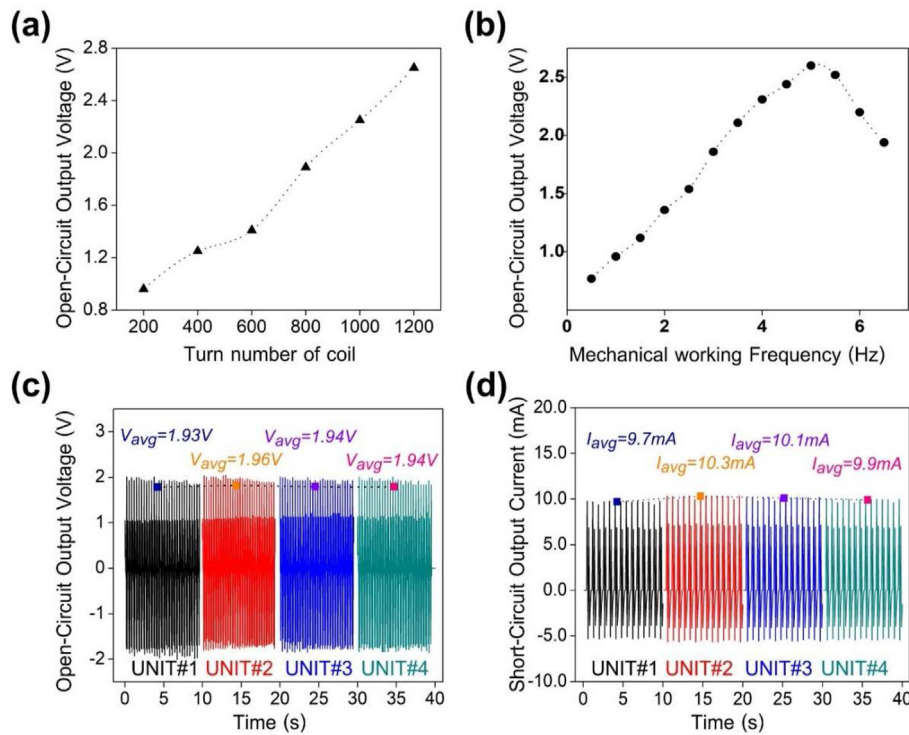

Fig. 7. Relationship between the maximum output of the open-circuit output voltage and the number of turns in the Cu coils (a), maximum output of the open-circuit output voltage and various mechanical force frequencies (b), open-circuit output voltage (c), and short-circuit output current (d) of each hollow cylindrical coil.

parallel mode. Regarding the assembled EMG, the electrical output current showed a significant improvement of 3.8 times, when compared to the average output current of each hollow cylindrical tube. As seen in Fig. 8(a), the V_{OC} and I_{SC} show maximum values of ~2.04 V and ~38 mA, respectively. Finally, the P was studied as the relationship of V_{DC}, I_{SC} and various external load resistances from 10 to 10 kΩ, as shown in Fig. 8(b). The V_{DC} increased and the I_{DC} decreased with increasing external load resistance, which corresponded to Ohmic law. The maximum P output of ~10.2 mW was obtained at the external load resistance of 30 Ω, which corresponded to the internal load resistance of the EMG.

3.2.3. Output performance of the hybrid hexagonal multilayer-shaped MO-CTENG and EMG

Regarding the internal impedance of the two power sources, the hexagonal multilayer-shaped MO-CTENG and EMG have a big difference, which affects the electrical output characteristic during series and parallel connection. To explore the electrical output characteristic of the MO-CTENG-EMG clearly, the devices were investigated systematically to validate the P by employing a series and parallel connections, as the circuit diagram shows in Fig. 9 (a). Both nanogenerator devices; the hexagonal multilayer-shaped MO-CTENG and EMG were stimulated by external force in the same period, with vertical contact-separation motion. The experimental setup for external force excitation is shown in Supplementary Fig. S6. A rectangular acrylic plate with a dimension of 20×9 cm^2 was used to excite the external force by the ACM. It was mounted between the rod holder and the hexagonal multilayer-shaped MO-CTENG and EMG. Regarding ideal current and voltage sources, the current source has infinite internal resistance, and output current is independent of external load. Whereas, the voltage source has zero internal resistance, and output voltage is independent of external load. Therefore, it might be noted that the characteristic of the hexagonal multilayer-shaped MO-CTENG and EMG makes them current and voltage sources, respectively. If the hexagonal multilayer-shaped MO-CTENG is connected to the EMG in parallel, in the experimental setup, the output voltage and current are handled in the external load by the EMG. On the other hand, if the hexagonal multilayer-shaped MO-CTENG is connected to the EMG in series, the output voltage and current are handled in the external load by the hexagonal multilayer-shaped MO-CTENG. This could be validated by the output P characteristic, which shows the internal load resistance matching the external load resistance at the maximum output P. The instantaneous output P characteristic of the hexagonal multilayer-shaped MO-CTENG and EMG is exhibited in parallel connection (blue line) in Fig. 9(b). The maximum output P was calculated from the relationship of P = IV by measuring the V_{DC} at various external load resistances, from 10 Ω to 1 MΩ. The maximum output P of ~10.04 mW was obtained

at an external load resistance of 30 Ω, and the measured V_{DC} was 2.17 V at saturation value. The measured data show a close identity to the EMG, confirming that parallel connection of the hexagonal multilayer-shaped MO-CTENG and EMG is closely equivalent to the EMG for the external load. Similarly, the instantaneous output P characteristic of the hexagonal multilayer-shaped MO-CTENG and EMG was measured in series connection (red line) and plotted as a function of external load resistance. The maximum output P of 9.04 mW was achieved at an external load resistance of 6 MΩ, and the maximum output I_{DC} of 55.3 μA was obtained, indicating that the series connection of the hexagonal multilayer-shaped MO-CTENG and EMG is closely equivalent to the hexagonal multilayer-shaped MO-CTENG alone for the external load. Therefore, it could be concluded that the parallel and series connections of two nanogenerators represented the voltage and current sources, respectively.

In order to further validate the electrical output characteristic of the MO-CTENG-EMG in real practical application, the devices between the hexagonal multilayer-shaped MO-CTENG and EMG were stacked in layers to minimize sizing for a portable device. After that, external force was applied in vertical contact-separation motion by human mechanical shaking. Thus, the external force would be motivated to the hexagonal multilayer-shaped MO-CTENG and EMG. Fig. 9(c) shows the response pattern of the output voltage signal waveform for two nanogenerator devices in the same period within one cycle of the contact-separation motion. Two peaks ($+P_1$ and $-P_2$) in the triboelectric signal and four ($-P_3$, $+P_4$, $-P_5$, and $+P_6$) in the electromagnetic signal were observed clearly, which displayed complicated signals in one cycle of contact-separation motion. The $+P_1$ signal waveform was generated during releasing motion, while the $-P_2$ signal waveform was generated during pressing motion. Likewise, the $-P_3$ and $+P_4$ signal waveforms were generated during pressing motion, while the permanent magnet moved downwards towards and away from the Cu coil, simultaneously. After releasing motion, the $-P_5$ and $+P_6$ signal waveforms were generated, while the permanent magnet moved backward and toward its original position. Moreover, the output signal waveform between the TENG/PENG and electromagnetic signal waveforms is opposite in the starting period, which might affect entire output voltage efficiency during the combination of a signal waveform.

Generated electrical energy typically needs to be stored in energy storage devices such as capacitors or batteries before supplying stored energy to the external load. To achieve a high electrical output characteristic, and avoid this issue, two full-bridge rectifiers were used to isolate the output voltage signal waveform from the TENG/PENG and EMG phenomena, as exhibited in Fig. 9(d). The positive and negative output voltage terminals (red and blue lines) of two full-bridge rectifiers were connected in parallel mode. The
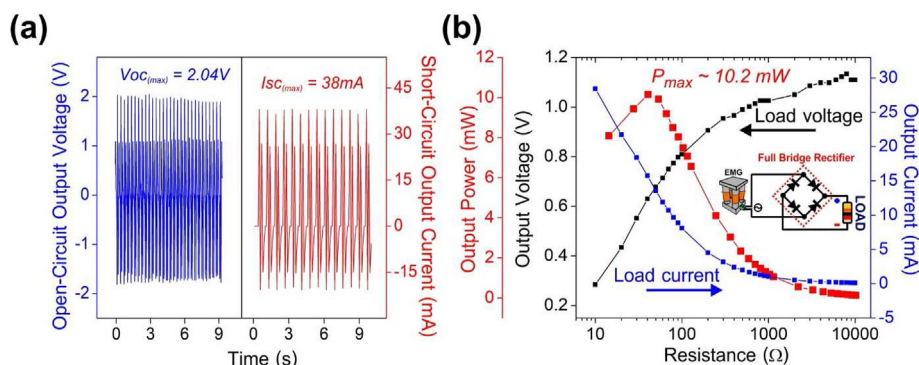

Fig. 8. Open-circuit output voltage and short-circuit output current (a), and instantaneous output power (b) of the assembled EMG.
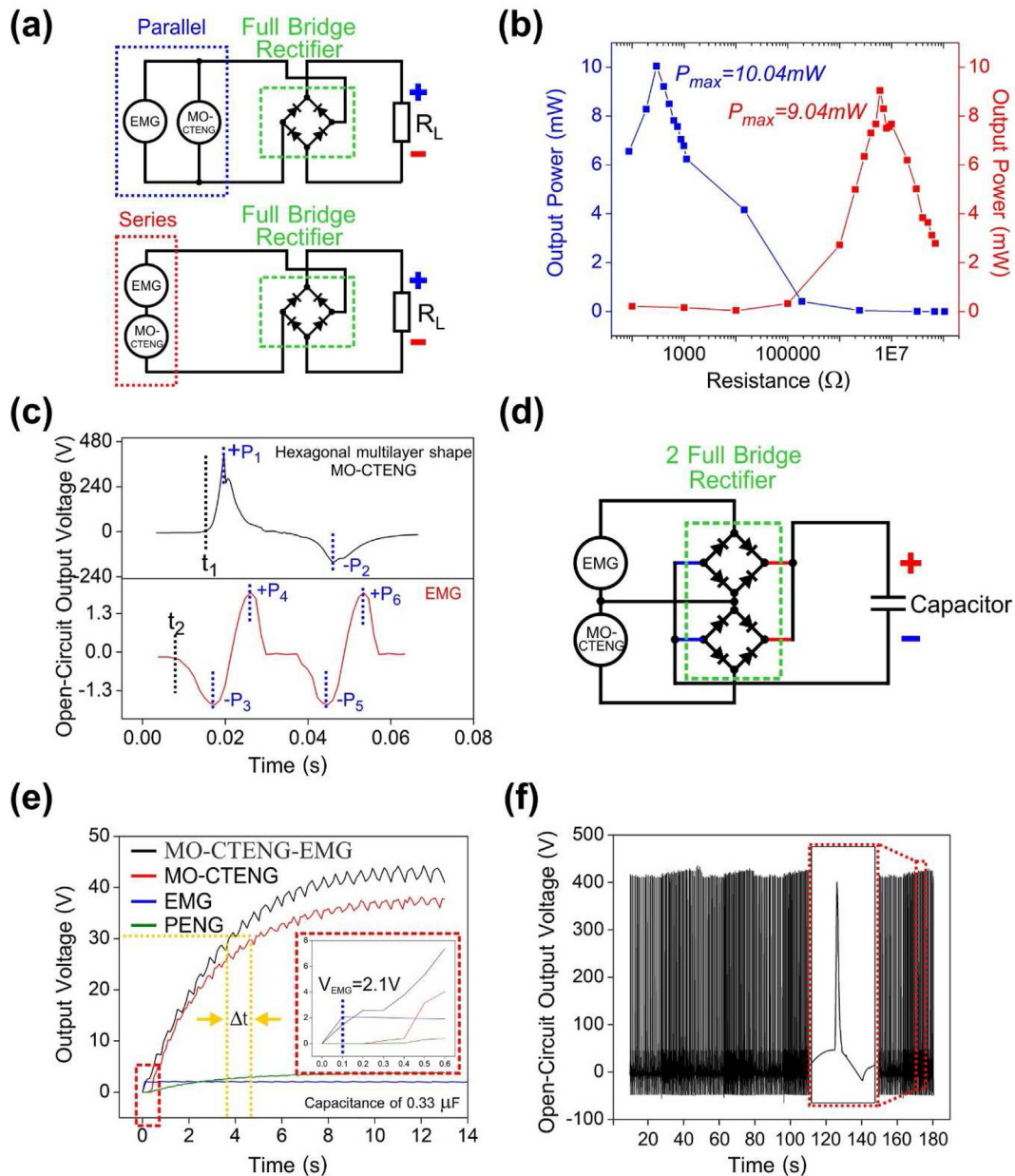
Fig. 9. Circuit diagram in parallel and series connections (a), instantaneous output power of the MO-CTENG-EMG in parallel and series connections (b), response pattern of the output voltage signal waveform of the MO-CTENG-EMG in the same period within one cycle of the contact-separation motion (c), circuit diagram of two full-bridge rectifiers (d), chargeability of the MO-CTENG-EMG, hexagonal multilayer-shaped MO-CTENG, EMG, and PENG with two full-bridge rectifiers (e), and output voltage stability of the MO-CTENG-EMG (f).

chargeability of different nanogenerator devices was validated, namely the MO-CTENG-EMG, hexagonal multilayer-shaped MO-CTENG and EMG. The capacitor of 0.33 μF was used in the experiment to validate the chargeability by measuring V_{DC}, as shown in Fig. 9(e). The charging speed of the EMG is faster in the starting period than the hexagonal multilayer-shaped MO-CTENG, MO-CTENG-EMG, and PENG because there are more transferred charges. This clearly revealed that the EMG could increase the speed of chargeability. After combining the hexagonal multilayer-shaped MO-CTENG and EMG, with two full-bridge rectifiers, the saturated output voltage is remarkably higher than that in the EMG and hexagonal multilayer-shaped MO-CTENG. The saturated voltage of 42.1 V and 35.7 V was obtained from the MO-CTENG-EMG and hexagonal multilayer-shaped MO-CTENG, respectively.

Moreover, the charging time of the MO-CTENG-EMG was lower at the same output voltage level of 30 V than that of the hexagonal multilayer-shaped MO-CTENG ($\Delta t = 1.1$ s), which could charge within 3.8 s. This indicates that the MO-CTENG-EMG is a better strategy for harvesting energy. Finally, the long-term ability test of the MO-CTENG-EMG was investigated in order to confirm stability of the output signal and durability of the hexagonal multilayer-shaped MO-CTENG, as shown in Fig. 9(f). The V_{DC} signal waveform shows no significant change in all testing periods.

Based on the authors' previous publication [26] on the 3D multi-layer Origami-TENG (O-TENG) structure, deterioration of structural design in the long-term ability test, by folding two perpendicularly arranged rectangular pieces of paper alternately, is a disadvantage in terms of electrical output performances, due to high-stress

concentration at the corner of the crease, which corresponds with Supplementary Fig. S7. This exhibits comparison of mechanical responses between the structure of the hexagonal multilayer-shaped MO-CTENG and 3D multi-layer O-TENG during contact-separation motion. The structural 3D multi-layer O-TENG exhibits a coupled twist along the central axis when stretching, because of interactions between the alternate folding of two paper ribbons. As a result, high-stress concentration appears near the corners of the creases, resulting in damage. On the other hand, the hexagonal multilayer-shaped MO-CTENG exhibits mechanical responses in linearity with no twist involved. Moreover, it shows more advantages in terms of flexibility, rigidity, self-stretching and elasticity. In order to show the advantage of the proposed structure, mechanical responses of both structures: 3D multi-layer O-TENG and hexagonal multilayer-shaped MO-CTENG, were compared systematically, as shown in Supplementary Movie, M1.

4. Practical application of the MO-CTENG-EMG for the self-powered wireless Global Positioning System (GPS)

To examine the excellent electrical output from the MO-CTENG-EMG, an external load of the GPS module (GY-NEO-6MV2 model) was selected to validate the electrical output characteristic in terms of powering source capability. Fig. 10 shows the working principle of the MO-CTENG-EMG for the self-powered wireless GPS. It consists of two main parts, namely the receiver and transmitter. As a receiver, a laptop and microcontroller unit (MCU; Arduino Nano) were used for data monitoring and data processing, respectively. The NRF24L01 wireless module could be executed like a receiver and transmitter of data and used for data communications of both parts. The amplifier circuit inside the NRF24L01 module, and an additional antenna, were applied to enhance efficiency of the communication wireless, which could operate from 1000 m away.

Similarly, the transmitter part was used in the MCU of Arduino Nano for data processing and transmitting data with the NRF24L01 wireless module. In order to carry innovation of the MO-CTENG-EMG easily, the hexagonal multilayer-shaped MO-CTENG and EMG were stacked in layers and placed inside a hexagonal prism of the built acrylic frame, shown in the schematic diagram of the transmitter part. The circuit design was constructed inside the top of the hexagonal prism. As for the circuit diagram of the

transmitter, the electrical output terminal wire of the two full-bridge rectifiers was connected in parallel and bonded to the 0.33 μF electrolyte capacitor for adjusting the ripple output voltage. Both rocker switches; switch number 1 and 2, were used respectively to validate intrinsic electrical output characteristic, and disconnect the battery unit during the electrical output measurement. A lead-sheet actuator (thickness ~0.7 cm with weight of ~500 g) was installed onto the hexagonal multilayer-shaped MO-CTENG to drive mechanical force by shaking from human motion. Finally, acrylic lids in the dimensions of the transmitter part were used to seal the hexagonal prism frame at the top and bottom of the acrylic frame. Owing to the desire for consistent power consumption of the MCU and wireless module, the lithium-ion battery of 3.7 V capacity with 250 mAh was applied for operation. Therefore, the wireless GPS system could track and locate information by connecting the rocker switch number 2 after 30 s had passed. The working principle of the MO-CTENG-EMG for the self-powered wireless GPS system is shown in Supplementary Movie, M2. Every 1 s, the located information; including the latitude and longitude, was transmitted from transmitter to receiver via the NRF24L01 wireless module. Then, the located information was processed by the MCU of the receiver part and displayed on the monitor via a serial monitoring port. Afterward, the received information was checked from Google to find the location. However, to demonstrate the intrinsic electrical output characteristic of the proposed portable self-powered source device, chargeability was examined by shaking from human motion. Rocker switches 1 and 2 were disconnected during electrical measurement to monitor the stored charges. The maximum V_{DC} of ~30 V could be achieved within 19 s. The saturation voltage of the capacitor reached only ~30 V when the external force was actuated by human mechanical shaking, compared with 42.1 V when external force was actuated by the ACM. This was because the variation of pressure force affects contact efficiency. Moreover, the frequency of mechanical force from human motion directly relates to electrical output performance of the EMG, which is in accordance with the experimental results in the previous section. Therefore, this might indicate that reduced V_{DC} corresponded to these phenomena. However, based on the relationship of $Q = CV$, Q is the stored charge, C is the capacitance, and V is the voltage. The stored charge at the maximum output voltage of ~30 V could obtain 9.9 μC for chargeability. This
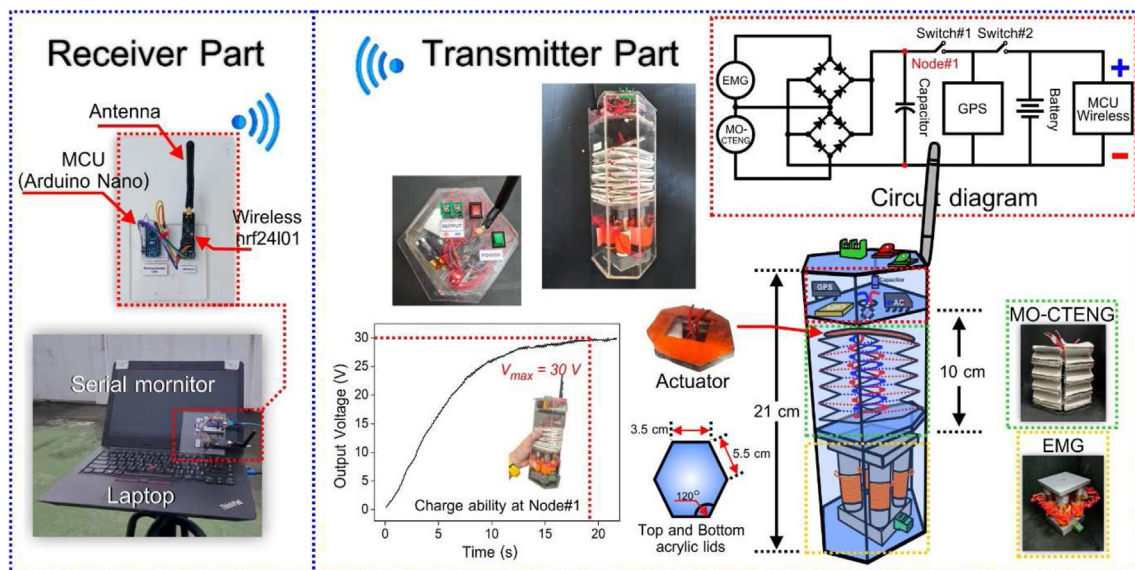

Fig. 10. Working principle of the MO-CTENG-EMG for self-powered wireless GPS system.

means that the stored charge of 9.9 μC from the capacitor would be transferred to a lithium-ion battery every ~19 s, when the saturated output voltage of the capacitor was obtained. On the other hand, if the constant mechanical force is performed continuously with a generated I_{SC} of ~38 mA, the battery charging time could be calculated from the fraction between battery capacity (250 mAh) and charging current. Therefore, the energy storage devices would be fully charged in around 6.5 h. To verify the self-charging and discharging mechanism of a lithium-ion battery, all external loads, except for the lithium-ion battery itself, were disconnected from the MO-CTENG-EMG device. The circuit diagram in Supplementary Fig. S8 (a) illustrates this setup. Upon applying a mechanical force generated by human motion to the MO-CTENG-EMG device, its voltage surged from approximately 3.7 V to around 26.8 V within a span of 19 s. Once the charging process was completed, the device was discharged while maintaining a constant stored charge of 8.8 μC. Consequently, the voltage decreased back to 3.7 V, as depicted in Supplementary Fig. S8 (b).

5. Conclusion

This study focused on the development of a mass-producible, eco-friendly, and high-performance nanogenerator that harvests mechanical energy to charge a battery in a wireless GPS system sustainably during human shaking motion. The nanogenerator integrated three phenomena, namely triboelectric, piezoelectric and electromagnetic, and used lead-free piezoelectric BT-NPs for 10 wt % to optimize the BC-based triboelectric composite film. Inspiration from the ancient art of the MO folding process was adapted to fabricate the hexagonal multilayer-shaped MO-CTENG for increasing the contact surface area. It demonstrated rigidity, durability, and flexibility with a self-sustained spring structure and showed a mechanical response with no twist involved during the stretching motion. This led to low resistant damage at the corner of the crease in the structure. The electrical output of ~414 V of V_{OC}, ~48.3 μA of I_{SC}, and ~6.94 mW of maximum P was obtained. Furthermore, the optimized EMG was fabricated to promote the I_{SC}, which displayed the highest value of ~38 mA, V_{OC} of ~2.04 V, and maximum P of ~10.2 mW. The MO-CTENG-EMG is characterized, based on two different electricity generating principles of parallel and series connections, corresponding to the equivalent circuit of ideal voltage and current sources, respectively. The complicated signal waveform from the EMG and hexagonal multilayer-shaped MO-CTENG also was focused on and managed by two full-bridge rectifiers that can store charges with a V_{DC} of 42.1 V within 8 s. Finally, the practical application of the MO-CTENG-EMG for the self-powered wireless GPS system was demonstrated successfully, and the sustainability of the self-powered device was displayed from mechanical harvesting by human motion, showing a V_{DC} of ~30 V within 19 s. The outcomes of this work provide an alternative way of achieving the highest electrical output characteristic from a nanogenerator in modern electronic technology.

Declaration of competing interest

The authors declare that they have no known competing financial interests or personal relationships that could have appeared to influence the work reported in this paper.

Acknowledgements

Appendix A. Supplementary data

References

[1] Z.L. Wang, Entropy theory of distributed energy for internet of things, Nano Energy 58 (2019) 669–672, https://doi.org/10.1016/j.nanoen.2019.02.012.

[2] X. Chen, L. Gao, J. Chen, S. Lu, H. Zhou, T. Wang, A. Wang, Z. Zhang, S. Guo, X. Mu, Z.L. Wang, Y. Yang, A chaotic pendulum triboelectric-electromagnetic hybridized nanogenerator for wave energy scavenging and self-powered wireless sensing system, Nano Energy 69 (2020) 104440, https://doi.org/10.1016/j.nanoen.2019.104440.

[3] X. Chen, X. Ma, W. Ren, L. Gao, S. Lu, D. Tong, F. Wang, Y. Chen, Y. Huang, H. He, B. Tang, J. Zhang, X. Zhang, X. Mu, Y. Yang, A triboelectric nanogenerator exploiting the Bernoulli effect for scavenging wind energy, Cell Rep. Phys. Science 1 (9) (2020) 100207, https://doi.org/10.1016/j.xcrp.2020.100207.

[4] A. Anderson, B. Rezaie, Geothermal technology: trends and potential role in a sustainable future, Appl. Energy 248 (2019) 18–34, https://doi.org/10.1016/j.apenergy.2019.04.102.

[5] D. Wöhrle, D. Meissner, Organic solar cells, Adv. Mater. 3 (3) (1991) 129–138, https://doi.org/10.1002/adma.19910030303.

[6] N. Saurabh, R. Kiran, S. Patel, Solar energy harvesting using lead-free pyro-electric bulk ceramics: a simulation study, J. Sci.: Adv. Mater. Dev. 8 (1) (2023) 100527, https://doi.org/10.1016/j.jsamd.2022.100527.

[7] Y. Shen, K. Lu, Scavenging power from ultra-low frequency and large amplitude vibration source through a new non-resonant electromagnetic energy harvester, Energy Convers. Manag. 222 (2020) 113233, https://doi.org/10.1016/j.enconman.2020.113233.

[8] P. Maharjan, T. Bhatta, M. Salauddin Rasel, M. Salauddin, M. Toyabur Rahman, J.Y. Park, High-performance cycloid inspired wearable electromagnetic energy harvester for scavenging human motion energy, Appl. Energy 256 (2019) 113987, https://doi.org/10.1016/j.apenergy.2019.113987.

[9] L. Zhou, D. Liu, J. Wang, Z.L. Wang, Triboelectric nanogenerators: fundamental physics and potential applications, Friction 8 (3) (2020) 481–506, https://doi.org/10.1007/s40544-020-0390-3.

[10] N. Sezer, M. Koç, A comprehensive review on the state-of-the-art of piezo-electric energy harvesting, Nano Energy 80 (2021) 105567, https://doi.org/10.1016/j.nanoen.2020.105567.

[11] M.R. Sarker, S. Julai, M.F.M. Sabri, S.M. Said, M.M. Islam, M. Tahir, Review of piezoelectric energy harvesting system and application of optimization techniques to enhance the performance of the harvesting system, Sens. Actuator A Phys. 300 (2019) 111634, https://doi.org/10.1016/j.sna.2019.111634.

[12] G. Miao, S. Fang, S. Wang, S. Zhou, A low-frequency rotational electromagnetic energy harvester using a magnetic plucking mechanism, Appl. Energy 305 (2022) 117838, https://doi.org/10.1016/j.apenergy.2021.117838.

[13] P. Carneiro, M.P. Soares dos Santos, A. Rodrigues, J.A.F. Ferreira, J.A.O. Simões, A.T. Marques, A.L. Kholkin, Electromagnetic energy harvesting using magnetic levitation architectures: a review, Appl. Energy 260 (2020) 114191, https://doi.org/10.1016/j.apenergy.2019.114191.

[14] F.-R. Fan, Z.-Q. Tian, Z. Lin Wang, Flexible triboelectric generator, Nano Energy 1 (2) (2012) 328–334, https://doi.org/10.1016/j.nanoen.2012.01.004.

[15] D. Hu, M. Yao, Y. Fan, C. Ma, M. Fan, M. Liu, Strategies to achieve high performance piezoelectric nanogenerators, Nano Energy 55 (2019) 288–304, https://doi.org/10.1016/j.nanoen.2018.10.053.

[16] B. Yan, N. Yu, L. Zhang, H. Ma, C. Wu, K. Wang, S. Zhou, Scavenging vibrational energy with a novel bistable electromagnetic energy harvester, Smart Mater. Struct. 29 (2) (2020) 025022, https://doi.org/10.1088/1361-665X/ab62e1.

[17] Y. Zhong, H. Zhao, Y. Guo, P. Rui, S. Shi, W. Zhang, Y. Liao, P. Wang, Z.L. Wang, An easily assembled electromagnetic-triboelectric hybrid nanogenerator driven by magnetic coupling for fluid energy harvesting and self-powered flow monitoring in a smart home/city, Adv. Mater. Tech. 4 (12) (2019) 1900741, https://doi.org/10.1002/admt.201900741.

[18] X. Wang, X. Liu, J. Zhang, L. Liang, M. Li, H. Yao, T. Hou, Y. Wu, Y. Zi, H. Zheng, A high-applicability, high-durability wearable hybrid nanogenerator with magnetic suspension structure toward health monitoring applications, Nano Energy 103 (2022) 107774, https://doi.org/10.1016/j.nanoen.2022.107774.

[19] H. Wang, A. Jasim, X. Chen, Energy harvesting technologies in roadway and bridge for different applications — a comprehensive review, Appl. Energy 212 (2018) 1083–1094, https://doi.org/10.1016/j.apenergy.2017.12.125.

[20] S. Sriphan, N. Vittayakorn, Hybrid piezoelectric-triboelectric nanogenerators for flexible electronics: recent advances and perspectives, J. Sci.: Adv. Mater. Dev. 7 (2022) 100461, https://doi.org/10.1016/j.jsamd.2022.100461.

[21] T. Quan, X. Wang, Z.L. Wang, Y. Yang, Hybridized electromagnetic–triboelectric nanogenerator for a self-powered electronic watch, ACS Nano 9 (2015) 12301–12310, https://doi.org/10.1021/acsnano.5b05598.

[22] W. Wang, J. Xu, H. Zheng, F. Chen, K. Jenkins, Y. Wu, H. Wang, W. Zhang, R. Yang, A spring-assisted hybrid triboelectric–electromagnetic nanogenerator for harvesting low-frequency vibration energy and creating a self-powered security system, Nanoscale 10 (2018) 14747–14754, https://doi.org/10.1039/C8NR04276D.

[23] L. Fei, D. Sujan, Origami theory and its applications: a literature review, Int. J. Hum. Soc. Sci. 7 (2013) 229–233, https://doi.org/10.5281/ZENODO.1055421.

[24] M. Szymanska-Chargot, J. Cybulska, A. Zdunek, Sensing the structural differences in cellulose from apple and bacterial cell wall materials by Raman and FT-IR spectroscopy, Sensors 11 (6) (2011) 5543–5560, https://doi.org/10.3390/s110605543.

[25] H.-J. Kim, E.-C. Yim, J.-H. Kim, S.-J. Kim, J.-Y. Park, I.-K. Oh, Bacterial nanocellulose triboelectric nanogenerator, Nano Energy 33 (2017) 130–137, https://doi.org/10.1016/j.nanoen.2017.01.035.

[26] S. Pongampai, P. Pakawanit, T. Charoonsuk, N. Vittayakorn, Low-cost fabrication of the highly efficient triboelectric nanogenerator by designing a 3D multi-layer origami structure combined with self-charged pumping module, Nano Energy 90 (2021) 106629, https://doi.org/10.1016/j.nanoen.2021.106629.

[27] T. Charoonsuk, S. Pongampai, P. Pakawanit, N. Vittayakorn, Achieving a highly efficient chitosan-based triboelectric nanogenerator via adding organic proteins: influence of morphology and molecular structure, Nano Energy 89 (2021) 106430, https://doi.org/10.1016/j.nanoen.2021.106430.

[28] S. Sriphan, U. Pharino, T. Charoonsuk, P. Pulphol, P. Pakawanit, O. Khamman, W. Vittayakorn, N. Vittayakorn, T. Maluangnont, Tailoring charge affinity, dielectric property, and band gap of bacterial cellulose paper by multifunctional Ti_2NbO_7 nanosheets for improving triboelectric nanogenerator performance, Nano Res. 16 (2) (2023) 3168–3179, https://doi.org/10.1007/s12274-022-4957-3.

[29] S. Pongampai, T. Charoonsuk, N. Pinpru, P. Pulphol, W. Vittayakorn, P. Pakawanit, N. Vittayakorn, Triboelectric-piezoelectric hybrid nanogenerator based on $BaTiO_3$-Nanorods/Chitosan enhanced output performance with self-charge-pumping system, Compos. B Eng. 208 (2021) 108602, https://doi.org/10.1016/j.compositesb.2020.108602.

[30] Z. Yi, D. Liu, L. Zhou, S. Li, Z. Zhao, X. Li, Z.L. Wang, J. Wang, Enhancing output performance of direct-current triboelectric nanogenerator under controlled atmosphere, Nano Energy 84 (2021) 105864, https://doi.org/10.1016/j.nanoen.2021.105864.

[31] N. Satpute, M. Iwaniec, J. Iwaniec, M. Mhetre, S. Arawade, S. Jabade, M. Banaś, Triboelectric nanogenerator-based vibration energy harvester using bio-inspired microparticles and mechanical motion amplification, Energies (2023), https://doi.org/10.3390/en16031315.

[32] L. Xu, T.Z. Bu, X.D. Yang, C. Zhang, Z.L. Wang, Ultrahigh charge density realized by charge pumping at ambient conditions for triboelectric nanogenerators, Nano Energy 49 (2018) 625–633, https://doi.org/10.1016/j.nanoen.2018.05.011.

[33] S. Niu, S. Wang, L. Lin, Y. Liu, Y.S. Zhou, Y. Hu, Z.L. Wang, Theoretical study of contact-mode triboelectric nanogenerators as an effective power source, Energy Environ. Sci. 6 (2013) 3576–3583, https://doi.org/10.1039/C3EE42571A.

[34] G. Zhu, C. Pan, W. Guo, C.-Y. Chen, Y. Zhou, R. Yu, Z.L. Wang, Triboelectric-generator-driven pulse electrodeposition for micropatterning, Nano Lett. 12 (2012) 4960–4965, https://doi.org/10.1021/nl302560k.

[35] D.W. Kim, J.H. Lee, J.K. Kim, U. Jeong, Material aspects of triboelectric energy generation and sensors, NPG Asia Mater. 12 (1) (2020), https://doi.org/10.1038/s41427-019-0176-0.